IEEE Access
Multidisciplinary | Rapid Review | Open Access Journal

Received June 23, 2021, accepted July 8, 2021, date of publication July 15, 2021, date of current version July 23, 2021.

Digital Object Identifier 10.1109/ACCESS.2021.3097545

The Effect of Drop Shape, Sensing Volume and Raindrop Size Statistics to the Scattered Field on 300 GHz

MIKKO KOKKONEN[1], HARRI JUTTULA[2], ANSSI MÄKYNEN[2], SAMI MYLLYMÄKI[1], AND HELI JANTUNEN[1]

[1]Microelectronics Research Unit, University of Oulu, 90014 Oulu, Finland
[2]Optoelectronics and Measurement Techniques Unit, University of Oulu, 90014 Oulu, Finland

Corresponding authors: Mikko Kokkonen (mikko.kokkonen@oulu.fi) and Harri Juttula (harri.juttula@oulu.fi)

This work was supported in part by the Academy of Finland 6G Flagship under Grant 318927, in part by the European Territorial Cooperation (ETC) Program Interreg V. A. Nord through the European Regional Development Fund (ERDF) under Grant NYPS 20202472, and in part by the Regional Council of Lapland under Grant 126/00.01.05.24.02/2019.

ABSTRACT Scattering and attenuation properties of rain using various drop models are calculated using Mie theory, the T-matrix method and numerical technique respectively. Ellipsoidal and oblate drops use the axis ratio of raindrops reported in literature. Scattering are presented both for small volumes containing a single drop and for large volumes with multiple drops in which the statistics of drop size distribution need to be taken into account. The angular dependence of scattering, absorption and scattering cross sections and polarization ratios are investigated. For single scattering the angular dependence and cross sections of nonspherical drops differed from those of a spherical drop. Differences between ellipsoid and oblate drops were minimal. Drop shape affected the polarization mostly at 40–140 degree detection angles. The averaged linear attenuation and rain induced cross channel signal were studied. Attenuation was close to the ITU-R.838 model and in the same order of magnitude as the attenuation due to atmospheric moisture. The cross channel signal was calculated as a function of rain rate and transmitter/receiver angle. Vertical polarization was observed to produce a higher cross channel signal than horizontal polarization. It was concluded that drop shape is not an important factor at 300 GHz due to small drops dominating the scattering signal. Overall, the results showed that in single scattering, the ellipsoid is a good approximation for raindrops and that for large volumes, a spherical drop approximation and a Mie solution may be sufficient at frequencies of 300 GHz and higher.

INDEX TERMS 6G, mie scattering, mmWave, raindrop, T-matrix.

I. INTRODUCTION

The terahertz (THz) band (0.1-1.0 THz) is a new unallocated radio band offering previously unattainable possibilities for future communication, sensing, and joint sensing-communications [1]–[8]. In communications, for example, sixth generation (6G) radio technology using the THz band is expected to enable hyper-fast links (1 Tbps) and extremely wide data bands up to 300 GHz. In localization and sensing, the millimeter (mmWave) technologies offer greater accuracy and are expected to promote applications such as fully autonomous vehicles [9], [10]. A typical sensor benefiting from higher frequencies is Frequency Modulated Continuous-Wave Radar (FMCW Radar) which is at the heart of many advanced driving assistance systems [11]–[13]. Research on automotive radar systems operating at 300 GHz is underway (Car2TERA project [14]).

Typically, radio frequencies are preferred over optical frequencies in radar and communication applications since they are not interfered with by adverse weather conditions like rain, fog or falling snow. So far, the effect of rain and other atmospheric particles has been studied using mainly the Mie solution in which the scatterers are assumed to be spherical [15]–[18]. Small drops such as cloud drops are known to be spherical, but falling raindrops are oblate due to the drag force of air. In the case of THz waves, the model used to represent the shape of a single raindrop may have a significant effect on wave propagation since

The associate editor coordinating the review of this manuscript and approving it for publication was Pavlos I. Lazaridis.

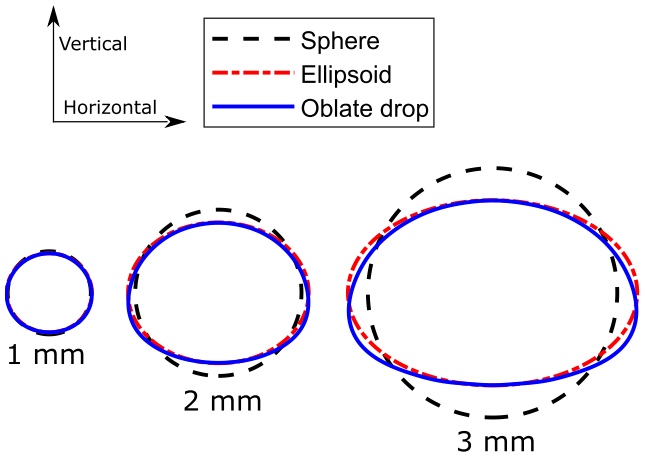

FIGURE 1. Cross sectional shapes of the volume equivalent drops (sphere, ellipsoid and oblate drop) with the radii of 1 mm, 2 mm and 3 mm. Definition of horizontal and vertical planes (polarization).

(i) the length of the electromagnetic wave is close to the size of the raindrop, (ii) the size distribution of raindrops has a large statistical variation at certain rain rates, and (iii) the asymmetrical oblate shape of the actual raindrop may have a substantial effect on the propagation of a polarized wave. In meteorology, for example, scattering by oblate drops is a well known phenomenon and forms the physical basis of modern dual polarization weather radars operating at S- and C-band frequencies [19].

In this work the freely falling raindrops have been modeled as spheres, ellipsoids, and oblate drops (Fig.1.) and the effect of these models on scattering and specific attenuation of 300 GHz polarized and unpolarized EM waves has been studied. The wave scattering was calculated using three different methods: Mie, T-matrix, and Finite Integration Technique (FIT). Mie and T-matrix are used for spheres and ellipsoids respectively while FIT was used for oblate drops. It was assumed that both the incident wave and the scattered wave propagate in the horizontal plane parallel to the ground. Consistency of the results was ensured by comparing the results of the different solutions for a sphere. The physical properties of the raindrop, the drop models used, and the methods are discussed in detail in the section II.

In this paper, effects related to large and small sensing volumes of natural raindrops using 300 GHz EM-waves are studied. The main questions are: (i) How does a single raindrop falling at terminal velocity affect the EM-wave scattering at 300 GHz (small sensing volume), and (ii) what is the significance of drop shape when there are multiple raindrops in the same sensing volume (large sensing volume). Answers to these questions are presented and discussed in the section III and conclusions of this study are offered in section IV.

II. THEORY AND METHODS

A. PHYSICAL PROPERTIES OF RAINDROPS

Raindrops are small nearly spherical atmospheric water particles in free fall. From the point of view of an EM wave raindrops are suspended in the air and they attenuate the propagating wave by scattering and absorption. In order to solve the scattering problem one needs to know the complex refractive index, size and shape of the raindrops.

The complex refractive index of water at 300 GHz is $n = 2.3989 + 1.0414i$ [20], where the real part is the refractive index which indicates the phase velocity of a wave and the imaginary part is the extinction coefficient which relates to the amount of attenuation when the wave passes through the medium.

The size and shape of the raindrops has been studied extensively [21]–[26]. The diameters of raindrops are typically between 0.1 mm and 6 mm. Small drops are typically more spherical while large drops are more flattened as depicted according to the model of Beard and Chuang [22] in Fig.1. Flattening is caused by the increased atmospheric drag of raindrops as their size increases.

In the context of scattering raindrops are usually assumed to be spheres. In this paper, the choice between spherical, elliptical or oblated (empirical) drop shape and its affect on the scattering of 300 GHz wave is compared. The drop shapes are referred to by their volume equivalent radius r_{eq} that simply defines a sphere with an equal volume of water. The shape of the elliptical drops can be solved by calculating the short axis a and the long axis b with the empirical axis ratio α [27]

$$\alpha = 1.0048 + 0.0057D - 2.628D^2 + 3.682D^3 - 1.677D^4, \tag{1}$$

where $D = 2r_{eq}$ is the diameter of a volume equivalent sphere in centimeters. The oblated drop is constructed as a solid of revolution of the cross section defined by [22]:

$$r(\phi) = r_0[1 + \Sigma c_n cos(n\phi)], \tag{2}$$

where $r(\phi)$ is the distance from the origin in the direction ϕ measured from the vertical axis defined in Fig. 1. The shape coefficients (c_n) for each drop size are presented in [22]. Examples of the cross sections of volume equivalent spherical, elliptical and oblated drop shapes with radii of 1 mm, 2 mm and 3 mm are shown in Fig. 1.

B. RAINDROP SIZE DISTRIBUTION

Raindrop size distribution $N(D)$ is defined as the number of raindrops with a diameter of $D + dD$ in unit volume of air as a function of drop diameter and rain rate. In this paper it is assumed that the raindrops obey the Weibull drop size distribution (DSD) [28]:

$$N(D) = N_0 \frac{\eta}{\sigma} \left(\frac{D}{\sigma}\right)^{\eta-1} e^{-\left(\frac{D}{\sigma}\right)^{\eta}} \tag{3}$$

Here D is the drop diameter and coefficients are $N_0 = 1000$, $\eta = 0.95R^{0.14}$, $\sigma = 0.26R^{0.44}$. Drop size distribution is hence a function only of rain rate R which is given in mm/h. In terms of rain, the rate rain can be described as light for up to 2.5 mm/h, moderate for up to 10 mm/h, heavy for up to 50 mm/h, and violent for larger than 50 mm/h. Besides the

Weibull distribution there are other known distributions. The selected DSD model may affect the average scattering and attenuation properties of rain [29], [30]. Naturally, effective drop size tends to have high natural variance. In addition, there are regional differences that affect the DSD model, for example, temperate and heavy rain regions tend to have more larger drops than smaller ones [31], [32].

C. SCATTERING OF EM WAVE BY SPHERICAL, ELLIPSOIDAL, AND OBLATE DROPS

1) SPHERE

The Mie solution describes the scattering of a plane wave from a spherical particle with a known complex refractive index. Interaction between the plane wave and a particle can be represented by extinction σ_{ext}, scattering σ_{sca} absorption σ_{abs} and backscattering σ_b cross sections [33]:

$$\sigma_{ext} = \frac{\pi D^2}{2x^2}\sum_{n=1}^{\infty}(2n+1)\Re(a_n+b_n) \tag{4}$$

$$\sigma_{sca} = \frac{\pi D^2}{2x^2}\sum_{n=1}^{\infty}(2n+1)(|a_n|^2+|b_n|^2) \tag{5}$$

$$\sigma_{abs} = \sigma_{ext} - \sigma_{sca} \tag{6}$$

$$\sigma_b = \frac{\pi D^2}{4x^2}\left|\sum_{n=1}^{\infty}(2n+1)(-1)^n(a_n-b_n)\right|^2 \tag{7}$$

Here D is the diameter of the particle, x is a size parameter defined as $x = \pi D/\lambda$ and a_n and b_n are the Mie coefficients for the scattered wave. Angular dependence of scattered radiation is given by the scattering phase function:

$$P(\theta) = \frac{|S_1(\theta)|^2 + |S_2(\theta)|^2}{\pi x^2 Q_{sca}}, \tag{8}$$

where $S_1(\theta)$ and $S_2(\theta)$ are the elements of the scattering amplitude matrix and Q_{sca} is the scattering efficiency. Scattering efficiency is defined simply by the ratio of the scattering cross section and geometrical cross section of the particle

$$Q_{sca} = \sigma_{sca}/A_{geom} \tag{9}$$

Extinction and absorption efficiencies can be similarly defined.

2) ELLIPSOID

Mie theory provides a solution only for homogeneous or layered spherical or infinitely long cylindrical particles and thus other method must be used for elliptical particles. T-matrix is another widely used method of solving scattering problems in the Mie resonance scattering regime and it is able to solve scattering by elliptical particles.

In the framework of the T-matrix method the incident $\mathbf{E_i}(\mathbf{r})$ and scattered fields $\mathbf{E_s}(\mathbf{r})$ represented with vector spherical harmonic functions $\mathbf{M}$ and $\mathbf{N}$ are:

$$\mathbf{E_i}(\mathbf{r}) = \sum_{nm}(a_{mn}^{(2)}\mathbf{M}_{mn}^{(2)}(k\mathbf{r}) + b_{mn}^{(2)}\mathbf{N}_{mn}^{(2)}(k\mathbf{r})) \tag{10}$$

$$\mathbf{E_s}(\mathbf{r}) = \sum_{nm}(p_{mn}^{(1)}\mathbf{M}_{mn}^{(1)}(k\mathbf{r}) + q_{mn}^{(1)}\mathbf{N}_{mn}^{(1)}(k\mathbf{r})) \tag{11}$$

Here the superscripts (1) and (2) refer to the degree of spherical Hankel functions. Expansion coefficients a_{nm} and b_{nm} of the incident wave are known and they are related to the coefficients of the scattered field p_{nm} and q_{nm} by a T-matrix:

$$\begin{bmatrix}\mathbf{p}\\ \mathbf{q}\end{bmatrix} = \mathbf{T}\begin{bmatrix}\mathbf{a}\\ \mathbf{b}\end{bmatrix} \tag{12}$$

In practice T-matrix calculations were solved with a Python interface that uses a Fortran implementation of the T-matrix method [34]. Details of the T-matrix method and its implementation can be found in [35]–[38].

With the T-matrix method, the ellipsoid approximation of a raindrop were used with axis ratios defined by (1) and calculated the absorption and scattering cross sections and angular dependence of the scattered wave were calculated in a horizontal plane. For very small drops the axis ratio of the drops approaches unity and the T-matrix solutions were checked for convergence with the predictions of the Mie theory.

3) OBLATE DROP

CST Studio Suite [39] was used to simulate scattering of the oblate drop shapes defined by (2). In the simulations either vertically or horizontally polarized plane wave excitation were used. FIT [40]–[43] was used to calculate radar cross sections and extinction parameters of the drops. Precision of the simulation was -80 dB and the hexahedral mesh was 60 per wavelength. Based on the CST manual, Radar Cross Section (RCS) is calculated by the following expression

$$RCS(\theta,\phi) = 4\pi\frac{\text{power radiated per unit angle}}{\text{stimulated power}} \tag{13}$$

and depends on the incident wave properties (polarization, propagation angle, frequency) and the target geometry and material properties. Calculations and simulations were performed for a single drop at a time. The smallest drop had an equivalent radius of 1 mm, and the radius was increased by 0.25 mm steps until the radius was 3 mm. Smaller than 1 mm radii were not calculated with CST because the solutions of CST and Mie theory converged.

III. RESULTS AND DISCUSSION

This section commences by introducing the scattering effects of a single drop. The angular dependence of scattering is presented for different drop shapes and sizes. Evolution of the scattering as a function of the volume equivalent radius is shown with a scattering asymmetry parameter. Scattering and absorption cross sections and backscattering coefficient are presented for a single drop as a function of the volume equivalent radius. After the scattering effects of single drops, the scattering by an ensemble of raindrops in the unit volume of air is taken into consideration. The specific attenuation for the different shapes at different rain rates is examined and compared with the ITU standard model. The average scattering angle by rain is presented for vertically and horizontally polarized incident waves.

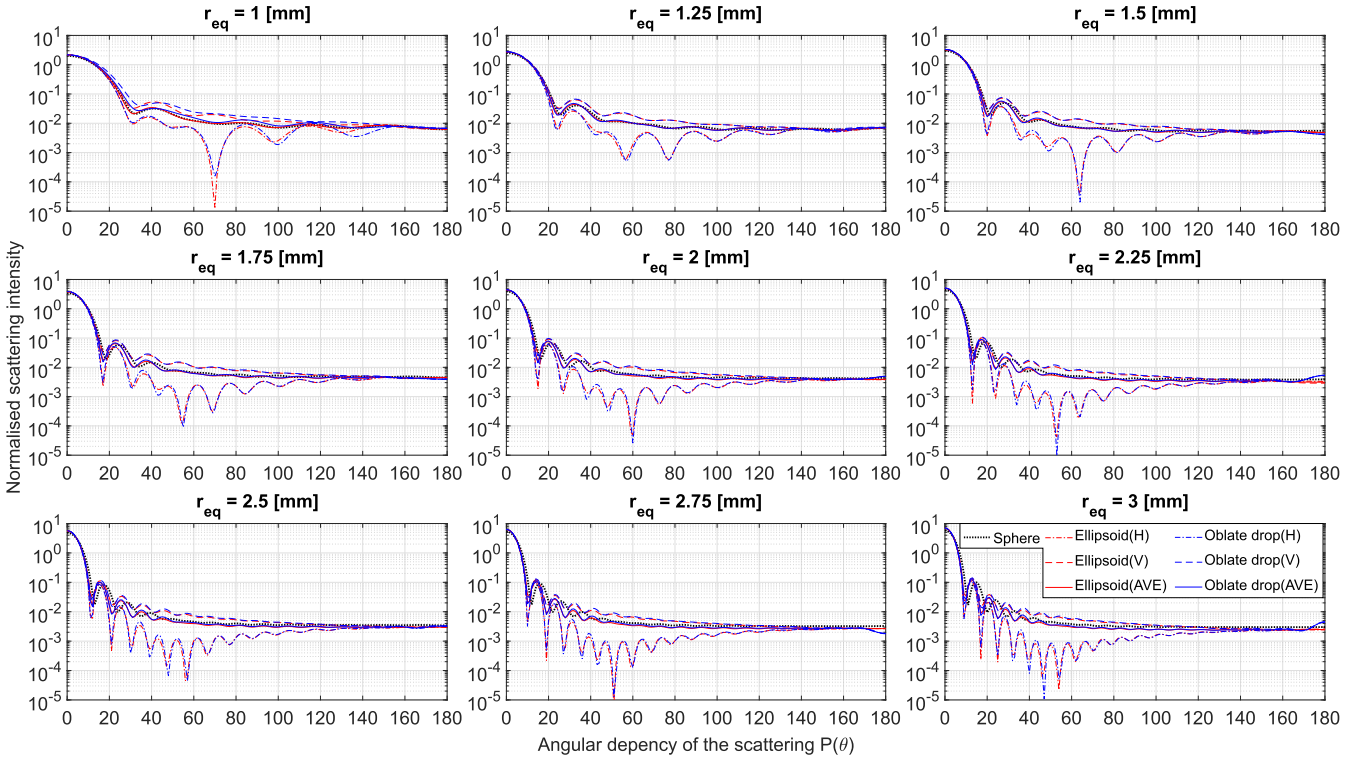

FIGURE 2. Angular dependence $P(\theta)$ of the scattered field of a sphere, an ellipsoid, and an oblate drop having volume equivalent radii between 1-3 mm. Horizontal polarization of the ellipsoid and the oblate drop clearly leads to lower scattering values and oscillates more than the sphere within the angular range of 20-120 degrees. Correspondingly the scattering values of vertical polarization of the ellipsoid and the oblate drop are higher. Also, the oscillation increases with increased size of the drop.

Directions of the polarizations are defined in Fig.1. Incident and scattered waves are assumed to propagate in a horizontal plane. Average attenuation and scattering are combined for a cross channel signal between the transmitter and the receiver with overlapping sensing cones. Finally, the extinction efficiency of a spherical drop at various radar frequencies is presented together with the raindrop size distribution.

A. ANGLE DEPENDENCE OF THE SCATTERING

Results of the calculations of the angular dependence $P(\theta)$ of the scattered plane wave in the cases of a sphere, ellipsoid and oblate drop are shown in Fig. 2. As the Mie theory predicted, scattering was strong in the forward direction $P(0)$ and weaker in other directions. The main lobe width of 1-mm drops was 60 degrees and their side lobe levels were below 0.1. When the drop size increased the main lobe became narrower as one would expect. A 3-mm drop had a main lobe width of only 20 degrees. Horizontal polarization (H) of the ellipsoid and the oblate drop lead to clearly lower scattering values and oscillated more than the sphere within the angular range of 20-120 degrees. Correspondingly the scattering values of vertical polarization (V) in the case of the ellipsoid and the oblate drop were higher than those of the sphere. This behavior seems logical due to the asymmetry of the ellipsoid and the oblate drop shapes.

Results for the ellipsoid and the oblate drop were close to each other and the average of the scattering values of horizontally and vertically polarized fields followed closely on those of the spherical drop.

Another way to examine the overall angular dependence of the scattered wave as a function of drop size is to represent scattering with the scattering asymmetry parameter g. Asymmetry is a dimensionless parameter that describes an expectation value for $cos(\theta)$, where θ is the scattering angle. For spherical particles, scattering asymmetry can be defined as [33]:

$$g = 2\pi \int_0^{\pi} P(\theta) cos(\theta) sin(\theta) d\theta \tag{14}$$

Here the scattering phase function $P(\theta)$ is normalized to result in unity when integrating over all scattering directions, $\int_0^{\pi} 2\pi P(\theta) sin(\theta) d\theta = 1$. In general, g can have values between -1 and 1 and $g = 1$ would mean all scattered energy is in the forward direction, $g = 0$ would describe symmetric scattering in both forward and backward direction and $g = -1$ would mean total backward scattering.

Scattering asymmetries for sphere, ellipsoid and oblate drop for H and V polarization fields are shown in Fig. 3. The Mie solution assumed the drop to be spherical and g was calculated for unpolarized incident radiation as defined in (14).

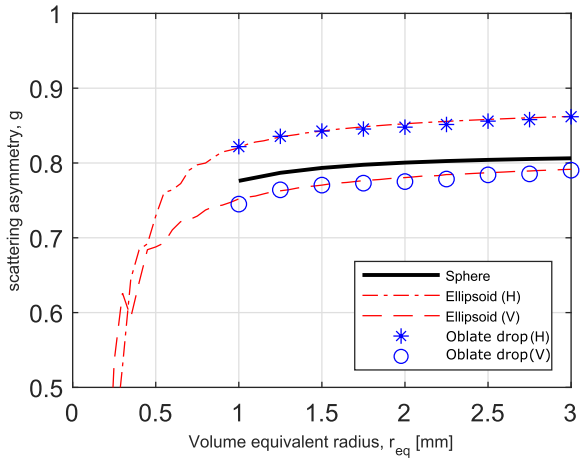

FIGURE 3. Asymmetry of the scattered EM field g for sphere, ellipsoid and oblate drop as a function of volume equivalent radius r_{eq}. Scattering asymmetry from the ellipsoid and the oblate drop follow each others closely. At small radii the scattering asymmetry approaches zero which indicates symmetric, Rayleigh type scattering.

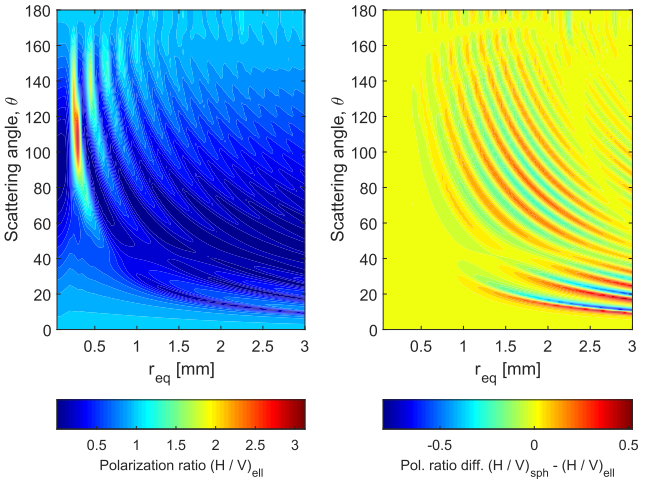

FIGURE 4. Polarization ratio for elliptical drop for unpolarized incident wave at different radii and scattering angles (left). Difference of polarization ratio of elliptical drop when compared to polarization ratio from spherical drop.

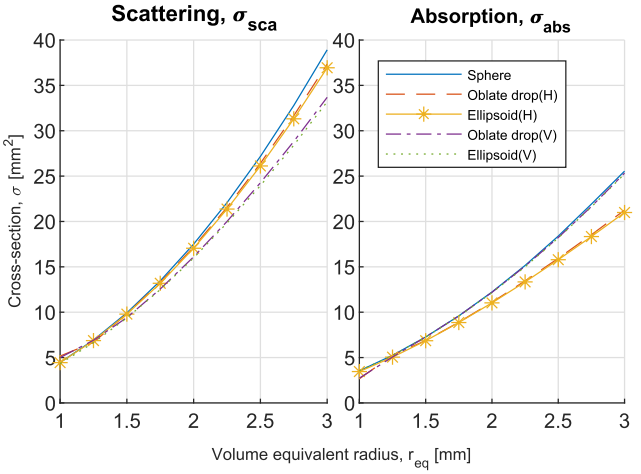

FIGURE 5. Scattering σ_{sca} and absorption σ_{abs} cross sections. Scattering cross section is larger for horizontal polarization for non spherical shapes while the reverse is true for absorption cross section.

The scattering in the forward direction was stronger for a horizontally polarized than for a vertically polarized incident field. In general, both ellipsoid and oblate drop lead to a lower g for vertical polarization and a higher g for horizontal polarization when compared with the Mie solution of the spherical drops with unpolarized incident radiation. Asymmetry was nearly identical for the ellipsoid and the oblate drop. Below 0.5 mm radius the asymmetry of the T-matrix solution used for the ellipsoid dropped rapidly towards zero. This indicates that the angular distribution of scattering becomes isotropic as the Rayleigh scattering regime ($r_{eq} \ll \lambda$) is approached.

The polarization state of a scattered wave from an unpolarized incident wave depends on the size of the drop and the scattering angle. Figure 4 shows the ratio of horizontally and vertically polarized scattered components of an unpolarized incident wave and the difference in polarization when compared to the scattering caused by a spherical drop. The largest differences in polarization ratios between the elliptical and spherical drop models could be seen at grazing angles and at angles close to perpendicular to the incident wave. This may be of interest if rain is analyzed in the THz range with methods similar to polarization sensitive laser diffraction techniques [44].

B. EFFECT OF DROP SIZE ON THE SCATTERING CROSS SECTIONS

Figure 5 presents the scattering σ_{sca} and absorption σ_{abs} cross sections which show the interaction between vertically polarized (V) and horizontally polarized (H) incident plane waves with different sizes of water drops. At 300 GHz frequency, the scattering effect from the drops was higher than the absorption and the difference between them grew as the size of the drop increased.

With a 1 mm radius drops the polarization states had almost no difference but with increased drop radius differences started to appear.

For ellipsoid and oblate drops, the scattering cross section was higher for horizontally polarized while the absorption cross section was higher for a vertically polarized incident wave. Scattering and absorption behaved as could be expected from the non spherical drop shapes.

C. BACKSCATTERING COEFFICIENT

The behavior of the backscattering coefficient σ_b for spherical and ellipsoidal drops is presented in Fig. 6 for a horizontally polarized incident wave. For comparison, a Rayleigh approximation of backscattering coefficient for a sphere was calculated with [33]:

$$\sigma_b = \frac{\pi^5}{\lambda^4} \left| \frac{n^2 - 1}{n^2 + 2} \right|^2 D^6 \tag{15}$$

in which λ is the wavelength, n is the complex refractive index of water and D is the drop diameter. It can be seen that below 0.1 mm radius the Rayleigh approximation agrees

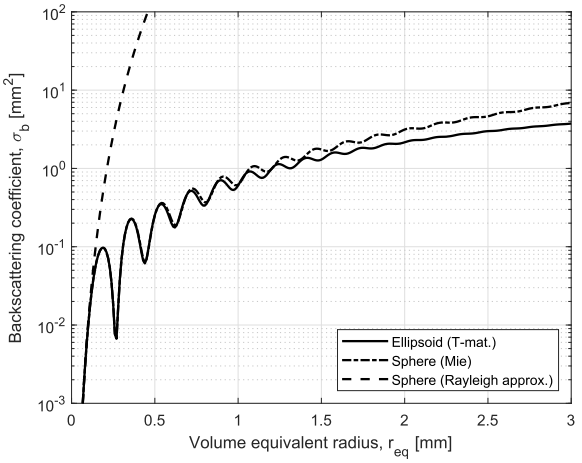

FIGURE 6. Backscattering coefficient for ellipsoidal and spherical raindrops with horizontally polarized incident radiation. The Rayleigh approximation for a spherical shape is shown for comparison.

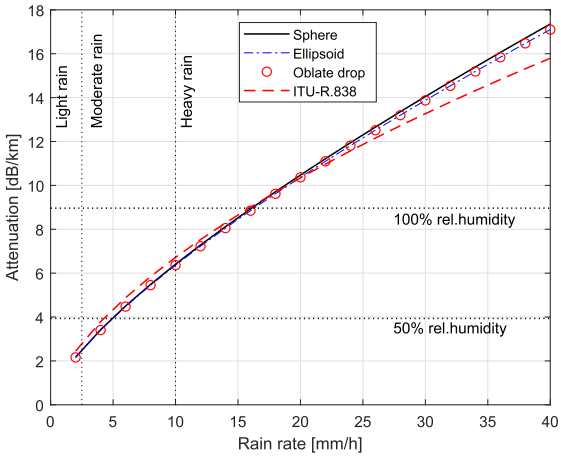

FIGURE 7. Specific attenuation at rain rates between 1 to 40 mm/h. For comparison, attenuation by atmospheric moisture is shown at 15°C temperature for 50% and 100% relative humidity with dashed lines.

with the Mie and T-matrix solutions but for $r > 0.1\lambda$ fails completely. This was expected and serves as a reminder that at 300 GHz and higher frequencies, raindrops don't satisfy the conditions of Rayleigh approximation. The backscattering coefficient σ_b was equal for sphere and ellipsoid up to approximately 1 mm radius and above that the ellipsoid had a slightly smaller backscattering coefficient. The difference is due to the fact that the ellipsoid treats the polarized incident wave differently as it gets more flattened with increasing volume equivalent radius. This should be considered for example if rain rate is analyzed from radar backscattering in THz applications.

D. RAIN AVERAGED SPECIFIC ATTENUATION

The scattering and absorption cross sections presented in Fig. 5 showed differences for a polarized wave in the cases of elliptical and oblate shaped drops. In order to evaluate their effect on path loss in rainy conditions the specific attenuation for the Mie and T-matrix solutions of spherical and elliptical drop shapes was calculated using the Weibull DSD according to (3) which provided a solution of the average extinction coefficient μ_{ext} for a given rain rate by calculating the integral

$$\mu_{ext} = \int_0^\infty \sigma_{ext}(D)N(D)dD \tag{16}$$

where the extinction cross section $\sigma_{ext} = \sigma_{abs} + \sigma_{sca}$ takes into account both absorption and scattering losses. For the oblate drop interpolated σ_{ext} values were used when solving the integral due to the sparse size data obtained using the CST solver.

If all absorbed and scattered radiation is considered lost, incident radiation obeys an exponential decay $I(z) = I_0 \exp(-\mu_{ext} z)$. Specific attenuation is presented in Fig. 7 in dB/km units for rain rates ranging from 2 to 40 mm/h including verbal descriptions of the rain intensity and the effect of atmospheric moisture. The extinction coefficient μ_{ext} was nearly identical for vertical and horizontal polarization and therefore only one solution is shown for the ellipsoid and oblate drop. Drop shape had minimal effect on specific attenuation when compared to the effect of atmospheric moisture which is shown with dashed lines for 50% and 100% relative humidity's at 15°C temperature. Calculated solutions were also close to the ITU-R838 attenuation model shown with a red dashed line [45].

Differences from the ITU model were so small that natural variations in DSD would probably have a larger effect on attenuation than drop shape. For example, at 10 mm/h rain rate the choice between different DSD models can easily increase or decrease the specific attenuation by 2 dB/km [29], [30]. In the case of linear attenuation the ITU model seems sufficient and by taking the drop shape into account no additional benefits are gained.

E. RAIN AVERAGED SCATTERING PHASE FUNCTION

The weighted averages of scattering phase functions were calculated over the full DSD range at three different rainrates from the T-matrix results. Results for both vertical and horizontal polarization are shown in Fig. 8. In this case scattering calculations were done for drops with equivalent radius between 0.01 - 3 mm with $\Delta r = 10\ \mu$m resolution before calculating the weighted average $\langle P(\theta)\rangle = \int P(\theta)N(D)dD$. Due to long calculation times, it was not possible to acquire similar results with CST with sufficient radial resolution (also, resolution for the drop shape is given at only 0.25 mm intervals [22]). An increasing rain rate could be observed to increase the proportion of forward scattering. This was expected because the proportion of small drops decreases relative to large drops with increasing rain rates. The largest differences between polarization states were observed between 60° and 80° scattering angles.

F. RAIN INDUCED SIGNAL FOR BISTATIC SENSOR

The rain averaged scattering phase functions for horizontal and vertical polarizations shown in Fig. 8 were used to

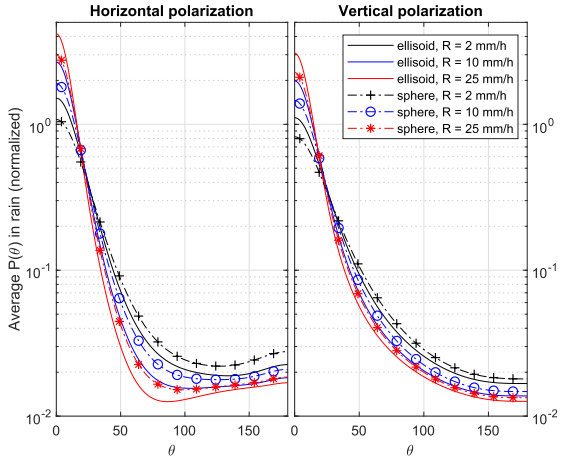

FIGURE 8. Scattering phase function of ellipsoid and sphere averaged over DSD for light (2 mm/h), moderate (10 mm/h), and heavy rain (25 mm/h). Increasing rain rate increases the proportion of forward scattering.

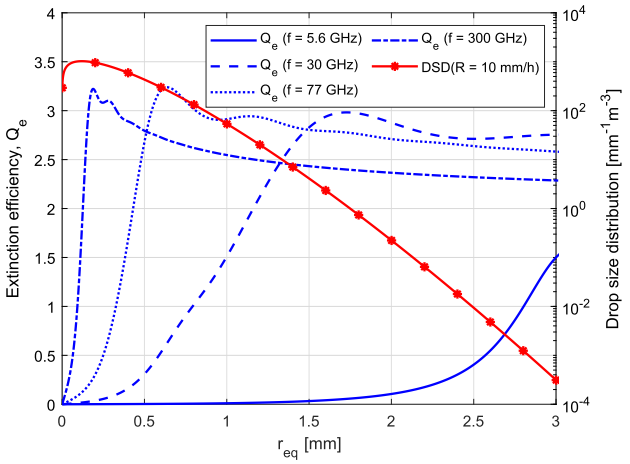

FIGURE 10. Left axis: extinction efficiency of spherical drop at various GHz frequencies. Right axis: drop size distribution (3) for 10 mm/h rain rate.

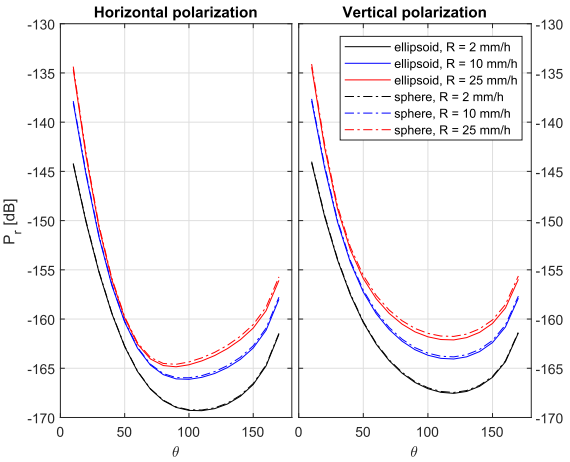

FIGURE 9. The rain induced cross channel signal between the transmitter and the receiver for vertical and horizontal polarizations. Transmitter and receiver are located at 50 m distance from the center of common volume of intersecting antenna cones at an angle θ.

demonstrate the cross channel signal due to rain at different rain rates in Fig. 9. This rain induced signal was calculated by numerically solving the bistatic radar equation over the intersecting volume of the transmitter and receiver antenna cones:

$$\frac{P_r}{P_t} = \frac{\lambda^2}{4\pi^3} \int \frac{G_t G_r}{(r_t r_r)^2} \eta(\theta_s) A_{air} A_{rain} dV \qquad (17)$$

Here P is power, λ is wavelength, G is antenna gain, r is distance to common volume. A scattering phase function was included in the bistatic scattering cross section $\eta(\theta_s)$. A_{air} and A_{rain} are attenuations due to air and rain respectively. Antenna gains were estimated with $G = -10log_{10}(0.5(1 - cos\theta))$ for constant cones with 2° half angles.

Calculation of the rain induced cross channel signal is described in more detail in our previous paper [30] where we used Mie scattering to estimate co-channel interference with a non-polarized incident wave. In Fig. 9 both transmitter and receiver were at 50 m distance from their intersecting antenna cones at different angles of incidence forming a 100 m long effective path length between Tx and Rx.

The cross channel signal mostly retained the shape of the rain averaged scattering phase function except when close to the backscattering angles where the signal increased if compared with the shape the of pure scattering phase function. This effect is explained by the fact that overlapping antenna cones lead to larger integration volumes in equation (17) near 0° and 180° Tx-Rx angles.

In general, a horizontally polarized incident wave seemed to cause less cross channel signal than vertical polarization. For this chosen geometry, at least, integration of equation (17) decreased the differences observed in Fig. 8. between spherical and elliptical drops which was due to a large proportion of nearly spherical small drops in DSD (3) that contributed to the total scattering. This can be seen clearly in Fig. 10 where the extinction efficiency Q_e of a sphere is shown for several GHz frequencies ranging from weather radar 5.6 GHz to 300 GHz frequencies side by side with the DSD for 10 mm/h rain.

IV. CONCLUSION

In general, electromagnetic scattering by spherical raindrops can be solved with Mie theory. However, large raindrops are not spherical due to atmospheric drag and their shape can be approximated with an ellipsoid or oblate drop. The T-matrix method and the finite integral technique were used in this paper to study the scattering properties of ellipsoidal and oblate drop approximations. We investigated both the single scattering case (small volume) and the scattering by a continuum of a large number of drops (large volume) with characteristic drop size distribution since different sensors and sensor networks can cover a wide range of different sensing volumes.

The effect of a single raindrop on the scattered field, cross sections and scattering parameters was investigated for small sensing volumes. The scattered field did not differ much between the ellipsoidal and oblate drop because the difference in their shapes was small, suggesting that an ellipsoidal shape is sufficient for the raindrop model. On the other hand, a difference between polarization states could be observed. A horizontally polarized incident wave had more forward oriented scattering distribution and on average had stronger scattering than that of a vertically polarized incident wave. Also, drop shape had a large impact on the polarization ratio at 40 to 140 degree range.

For large sensing volumes the rain averaged linear attenuation and the rain induced cross channel signal were studied assuming the raindrops to obey the well-known Weibull drop size distribution. Attenuation from the simulated raindrops was similar to the ITU-R838 model with only slight differences at heavy rain rates. On average, attenuation due to rain is of the same order of magnitude as attenuation due to typical air humidity ranges. For the cross channel signal, a difference between horizontal and vertical polarization around 50 to 150 degree was observed where the impact of the drop shape was barely visible.

With large volumes the impact from the oblate shape diminishes because the rain contains a larger number of small nearly spherical drops than large oblate drops. At 300 GHz or higher frequencies the small drops are effective scatterers and for large volumes the simple Mie approximation may be sufficient for scattering problems. In the case of small sensing volumes, the shape of the individual drops and rain rate can be detected.

These results could be used as a tool for engineers to develop new applications for 300 GHz.

REFERENCES

[1] M. Latva-Aho and K. Leppänen, Eds., "Key drivers and research challenges for 6G ubiquitous wireless intelligence," 6G Research Visions 1, Univ. Oulu, Oulu, Finland, Sep. 2019. [Online]. Available: http://urn.fi/urn:isbn:9789526223544

[2] T. S. Rappaport, Y. Xing, O. Kanhere, S. Ju, A. Madanayake, S. Mandal, A. Alkhateeb, and G. C. Trichopoulos, "Wireless communications and applications above 100 GHz: Opportunities and challenges for 6G and beyond," *IEEE Access*, vol. 7, pp. 78729–78757, 2019.

[3] M. A. Jamshed, A. Nauman, M. A. B. Abbasi, and S. W. Kim, "Antenna selection and designing for THz applications: Suitability and performance evaluation: A survey," *IEEE Access*, vol. 8, pp. 113246–113261, 2020.

[4] B. Paul, A. R. Chiriyath, and D. W. Bliss, "Survey of RF communications and sensing convergence research," *IEEE Access*, vol. 5, pp. 252–270, 2017.

[5] C. B. Barneto, S. D. Liyanaarachchi, M. Heino, T. Riihonen, and M. Valkama, "Full duplex radio/radar technology: The enabler for advanced joint communication and sensing," *IEEE Wireless Commun.*, vol. 28, no. 1, pp. 82–88, Feb. 2021.

[6] T. Kürner, D. M. Mittleman, and T. Nagatsuma, Eds., *THz Communications: Paving the Way Towards Wireless Tbps*, 1st ed. Cham, Switzerland: Springer, 2021.

[7] A. Ghavidel, S. Myllymäki, M. Kokkonen, N. Tervo, M. Nelo, and H. Jantunen, "A sensing demonstration of a subTHz radio link incorporating a lens antenna," 2021.

[8] A. Ghavidel, S. Myllymäki, M. Kokkonen, N. Tervo, and H. Jantunen, "Lens antenna adjustment for telecommunication and imaging modes in a sub-THz radio system," 2021.

[9] C. D. Lima, D. Belot, R. Berkvens, A. Bourdoux, A. Dardari, M. Guillaud, M. Isomursu, E.-S. Lohan, Y. Miao, A. N. Barreto, M. R. K. Aziz, J. Saloranta, T. Sanguanpuak, H. Sarieddeen, G. Seco-Grandados, J. Suutala, T. Svensson, M. Valkama, H. Wymeersch, and B. E. van Liempd, "6G white paper on localization and sensing," 6G Res. Vis., Univ. Oulu, Oulu, Finland, White Paper 12, 2020.

[10] N. Rajatheva, I. Atzeni, E. Björnson, A. Bourdoux, S. Buzzi, J.-B. Doré, S. Erkuck, M. Fuentas, K. Guan, T. Hu, X. Huang, J. Hulkkonen, J. M. Jornet, M. Katz, R. Nilsson, E. Panayirci, K. Rabie, N. Rajapaksha, M. Salehi, and W. Xu, "White paper on broadband connectivity in 6G," 6G Res. Vis., Univ. Oulu, Oulu, Finland, White Paper 10, 2020.

[11] M. Caris, S. Stanko, S. Palm, R. Sommer, A. Wahlen, and N. Pohl, "300 GHz radar for high resolution SAR and ISAR applications," in *Proc. 16th Int. Radar Symp.*, Dresden, Germany, Jun. 2015, pp. 577–580.

[12] E. Marchetti, R. Du, F. Norouzian, E. G. Hoare, M. Cherniakov, M. Gashinova, and T.-Y. Tran, "Radar reflectivity and motion characteristics of pedestrians at 300 GHz," in *Proc. Eur. Radar Conf.*, Nuremberg, Germany, Oct. 2017, pp. 57–60.

[13] D. Jasteh, E. G. Hoare, M. Cherniakov, and M. Gashinova, "Experimental low-terahertz radar image analysis for automotive terrain sensing," *IEEE Geosci. Remote Sens. Lett.*, vol. 13, no. 4, pp. 490–494, Apr. 2016.

[14] *Car2TERA*. Accessed: May 18, 2021. [Online]. Available: https://car2tera.eu/about

[15] U. A. Korai, L. Luini, R. Nebuloni, C. Capsoni, and D. Kapal, "Modeling statistics of rain attenuation affecting FSO links: A case study," in *Proc. 10th Eur. Conf. Antennas Propag.*, Davos, Switzerland, Apr. 2016, pp. 1–4.

[16] Q. Jing, D. Liu, and J. Tong, "Study on the scattering effect of terahertz waves in near-surface atmosphere," *IEEE Access*, vol. 6, pp. 49007–49018, 2018.

[17] F. Norouzian, E. Marchetti, M. Gashinova, E. Hoare, C. Constantinou, P. Gardner, and M. Cherniakov, "Rain attenuation at millimeter wave and low-THz frequencies," *IEEE Trans. Antennas Propag.*, vol. 68, no. 1, pp. 421–431, Jan. 2020.

[18] M. Tamošiūnaitė, V. Tamošiūnas, and G. Valušis, "Wireless communications beyond 5G: Uncertainties of terahertz wave attenuation due to rain," *Lithuanian J. Phys.*, vol. 58, no. 2, pp. 149–158, Jul. 2018.

[19] V. N. Bringi, *Polarimetric Doppler Weather Radar: Principles and Applications*. Cambridge, U.K.: Cambridge Univ. Press, 2001.

[20] D. J. Segelstein, "The complex refractive index of water," M.S. thesis, Dept. Phys., Univ. Missouri, Kansas City, MO, USA, 1981.

[21] J. E. McDonald, "The shape and aerodynamics of large raindrops," *J. Meteorol.*, vol. 11, no. 6, pp. 478–494, Dec. 1954.

[22] K. V. Beard and C. Chuang, "A new model for the equilibrium shape of raindrops," *J. Atmos. Sci.*, vol. 44, no. 11, pp. 1509–1524, 1987.

[23] F. Y. Testik, A. P. Barros, and L. F. Bliven, "Field observations of multimode raindrop oscillations by high-speed imaging," *J. Atmos. Sci.*, vol. 63, no. 10, pp. 2663–2668, Oct. 2006.

[24] M. Szakáll, K. Diehl, S. K. Mitra, and S. Borrmann, "A wind tunnel study on the shape, oscillation, and internal circulation of large raindrops with sizes between 2.5 and 7.5 mm," *J. Atmos. Sci.*, vol. 66, no. 3, pp. 755–765, Mar. 2009.

[25] K. V. Beard, V. N. Bringi, and M. Thurai, "A new understanding of raindrop shape," *Atmos. Res.*, vol. 97, no. 4, pp. 396–415, Sep. 2010.

[26] S. Müller, M. Szakáll, S. K. Mitra, K. Diehl, and S. Borrmann, "Shapes and oscillations of raindrops with reduced surface tensions: Measurements at the Mainz vertical wind tunnel," *Atmos. Res.*, vol. 119, pp. 38–45, Jan. 2013.

[27] K. Andsager, K. V. Beard, and N. F. Laird, "Laboratory measurements of axis ratios for large raindrops," *J. Atmos. Sci.*, vol. 56, no. 15, pp. 2673–2683, Aug. 1999.

[28] M. Sekine and G. Lind, "Rain attenuation of centimeter, millimeter and submillimeter radio waves," in *Proc. 12th Eur. Microw. Conf.*, Helsinki, Finland, Oct. 1982, pp. 584–589.

[29] S. Ishii, S. Sayama, and T. Kamei, "Measurement of rain attenuation in terahertz wave range," *Wireless Eng. Technol.*, vol. 2, no. 3, pp. 119–124, 2011.

[30] H. Juttula, J. Kokkoniemi, J. Lehtomaki, A. Mäkynen, and M. Juntti, "Rain induced co-channel interference at 60 GHz and 300 GHz frequencies," in *Proc. IEEE Int. Conf. Commun. Workshops (ICC Workshops)*, Shanghai, China, May 2019, pp. 1–5.

[31] H. Y. Lam, J. Din, and S. L. Jong, "Statistical and physical descriptions of raindrop size distributions in equatorial Malaysia from disdrometer observations," *Adv. Meteorol.*, vol. 2015, pp. 1–14, Apr. 2015.

[32] J. Ryu, H. Song, B. Sohn, and C. Liu, "Global distribution of three types of drop size distribution representing heavy rainfall from GPM/DPR measurements," *Geophys. Res. Lett.*, vol. 48, no. 3, Feb. 2021, Art. no. e2020GL090871.
[33] C. F. Bohren and D. R. Huffman, *Absorption and Scattering of Light by Small Particles*. New York, NNY, USA: Wiley, 1983.
[34] J. Leinonen, "High-level interface to T-matrix scattering calculations: Architecture, capabilities and limitations," *Opt. Exp.*, vol. 22, no. 2, pp. 1655–1660, Jan. 2014.
[35] P. C. Waterman, "Symmetry, unitarity, and geometry in electromagnetic scattering," *Phys. Rev. D, Part. Fields*, vol. 3, no. 4, pp. 825–839, Feb. 1971.
[36] M. I. Mishchenko and L. D. Travis, "T-matrix computations of light scattering by large spheroidal particles," *Opt. Commun.*, vol. 109, nos. 1–2, pp. 16–21, 1994.
[37] M. I. Mishchenko, L. D. Travis, and D. W. Mackowski, "T-matrix computations of light scattering by nonspherical particles: A review," *J. Quant. Spectrosc. Radiat. Transf.*, vol. 55, no. 5, pp. 535–575, 1996.
[38] D. J. Wielaard, M. I. Mishchenko, A. Macke, and B. E. Carlson, "Improved t-matrix computations for large, nonabsorbing and weakly absorbing nonspherical particles and comparison with geometrical-optics approximation," *Appl. Opt.*, vol. 36, no. 18, pp. 4305–4313, Jun. 1997.
[39] *CST*. Accessed: May 18, 2021. [Online]. Available: https://www.3ds.com/products-services/simulia/products/cst-studio-suite/
[40] T. Weiland, "A discretization method for the solution of Maxwell's equations for six-component fields," *AEU Int. J. Electron. Commun.*, vol. 31, no. 3, pp. 116–120, 1977.
[41] T. Weiland, "Time domain electromagnetic field computation with finite difference methods," *Int. J. Numer. Model. Electron. Netw., Devices Fields*, vol. 9, no. 4, pp. 295–319, 1996.
[42] B. Krietenstein, R. Schuhmann, P. Thoma, and T. Weiland, "The perfect boundary approximation technique facing the big challenge of high precision field computation," in *Proc. XIX Int. Linear Accel. Conf. (LINAC)*, Chicago, IL, USA, 1998, pp. 860–862.
[43] T. Weiland, "RF & microwave simulators—From component to system design," in *Proc. Eur. Microw. Week (EUMW)*, vol. 2, Munich, Germany, 2003, pp. 591–596.
[44] H. Li, J. Li, J. Bodycomb, and G. S. Patience, "Experimental methods in chemical engineering: Particle size distribution by laser diffraction—PSD," *Can. J. Chem. Eng.*, vol. 97, no. 7, pp. 1974–1981, Jul. 2019.
[45] *Specific Attenuation Model for Rain for Use in Prediction Methods*, document ITU-R P.838, ITU, Geneva, Switzerland, 2005.

MIKKO KOKKONEN received the bachelor's and master's degrees in physics from the University of Oulu, Oulu, Finland, where he is currently pursuing the Ph.D. degree with the Microelectronics Research Unit, Faculty of Information Technology and Electrical Engineering. His current research interests include use of new materials as an RF lens, solar panels, and green energy.

HARRI JUTTULA received the M.Sc. degree in physics from the University of Oulu, Oulu, Finland, in 2009. He is currently working as a Project Researcher with the Measurement Technology Research Unit, Kajaani, Finland. His research interests include CFD modeling and applications of scattering of light and electromagnetic radiation in industrial and environmental measurements.

ANSSI MÄKYNEN received the M.Sc. (Tech.) (Hons.) and D.Sc. (Tech.) degrees from the University of Oulu, Oulu, Finland, in 1987 and 2000, respectively. He is currently a Senior Research Fellow and the Research Group Leader with the Faculty of Information Technology and Electrical Engineering, University of Oulu. His current research interests include optical methods for industrial and environmental on-line inspection, especially characterization of materials using various imaging and spectroscopic methods.

SAMI MYLLYMÄKI received the M.Sc. and D.Sc. degrees from the University of Oulu, Oulu, Finland. He is currently the Research Group Leader and an Adjunct Professor with the Microelectronics Research Unit, Faculty of Information Technology and Electrical Engineering, University of Oulu. His research interests include microwave measurements, components and materials, and teaching includes electronics packaging technology.

HELI JANTUNEN has been the Group Leader of the Electronics Materials, Packaging, and Reliability Techniques Research Group, Infotech Oulu, Finland, since 2004. She is currently a Professor and the Head of the Microelectronics Research Unit, Faculty of Information Technology and Electrical Engineering, University of Oulu, Oulu, Finland. Her current research interests include the design, development, synthesis, implementation of electronics materials and their components for RF and microwave applications, and multifunctional micromodules.